ALL PATCHES MATTER, MORE PATCHES BETTER: ENHANCE AI-GENERATED IMAGE DETECTION VIA PANOPTIC PATCH LEARNING

Anonymous authors
Paper under double-blind review

ABSTRACT

The rapid proliferation of AI-generated images (AIGIs) highlights the pressing demand for generalizable detection methods. In this paper, we establish two key principles for AIGI detection task through systematic analysis: **(1) All Patches Matter**, since the uniform generation process ensures that each patch inherently contains synthetic artifacts, making every patch a valuable detection source; and **(2) More Patches Better**, as leveraging distributed artifacts across more patches improves robustness by reducing over-reliance on specific regions. However, counterfactual analysis uncovers a critical weakness: naively trained detectors display **Few-Patch Bias**, relying disproportionately on *minority patches*. We identify this bias to **Lazy Learner** effect, where detectors to limited patch artifacts while neglecting distributed cues. To address this, we propose **Panoptic Patch Learning** framework, which integrates: (1) *Randomized Patch Reconstruction*, injecting synthetic cues into randomly selected patches to diversify artifact recognition; (2) *Patch-wise Contrastive Learning*, enforcing consistent discriminative capability across patches to ensure their uniform utilization. Extensive experiments demonstrate that PPL enhances generalization and robustness across datasets.

1 INTRODUCTION

The rapid evolution of generative AI models has precipitated an exponential growth of AI-generated images (AIGIs) in digital ecosystems (Goodfellow et al., 2014; Karras et al., 2018; 2019; Ho et al., 2020; Rombach et al., 2022; Zhang et al., 2023; Ramesh et al., 2021; Yan et al., 2025; 2024c). This proliferation raises concerns regarding information security and content authenticity, highlighting the need for AIGI detection to distinguish synthetic images from authentic ones. Unlike conventional classification tasks, AIGI detection operates as a "*cat-and-mouse game*", presenting unique challenges due to: (1) continuous emergence of new generative architectures, and (2) frequent updates to existing generative models. Consequently, exhaustive training on all synthetic data becomes impractical (Ojha et al., 2023), thus necessitating detectors with strong generalizability.

Despite these challenges, AIGIs exhibit a distinctive property absent in traditional classification: Universal Artifact Distribution. In the context of AIGIs, discriminative features are not confined to object-centric regions; instead, *synthetic images contain artifacts uniformly across all patches, a consequence of the consistent generation process of modern generative models*.[1] This indicates that every patch contains synthetic traces, forming our first principle for AIGI detection: All Patches Matter. This principle is supported by two lines of evidence: (1) visual analytics (Tan et al., 2024c; Cozzolino et al., 2024) confirm pixel-level discriminative patterns, revealing artifacts at patch granularity; and (2) recent patch-wise detectors (Chen et al., 2024b; Zhong et al., 2024) demonstrate comparable performance to full-image approaches, validating the discriminative capability of individual patches. Although artifacts vary across patches, detectors that capture diverse artifacts across distributed regions reduce over-reliance on specific patches. Capturing these distributed artifacts

[1]This work adheres to the mainstream AIGI detection setting (Chen et al., 2024a; Ojha et al., 2023; Tan et al., 2024a; Liu et al., 2024; He et al., 2024; Zhu et al., 2024; Tan et al., 2024c) where the entire image is generated by AI models.

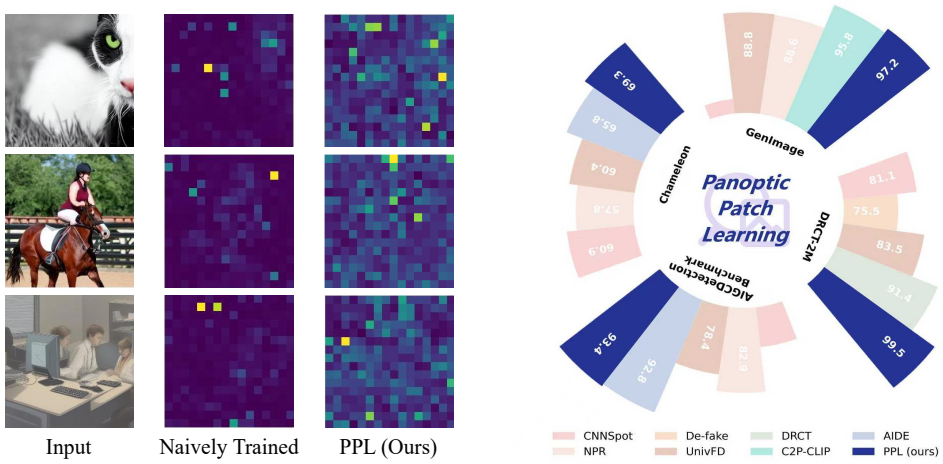

(a) Visualization of attention maps.

(b) Comparison on different datasets.

Figure 1: **(a)** PPL produces a more uniform attention distribution across patches, indicating its effectiveness in capturing artifacts comprehensively. **(b)** PPL outperforms peer methods on GenImage, DRCT-2M, AIGCDetectionBenchmark, and the in-the-wild Chameleon. More details are in Section 5.

enhances cross-generator generalizability by mitigating detectors' blind spots. This leads to our second principle: More Patches Better.

However, counterfactual analysis of existing AIGI detectors (Ojha et al., 2023; Liu et al., 2024; Tan et al., 2024a; He et al., 2024; Chen et al., 2024a) reveals an unfavorable tendency—Few-Patch Bias—supported by two empirical observations and a quantitative analysis. Empirically, we observe: (1) detectors' attention maps disproportionately focus on very limited patches; (2) detectors exhibit severe patch-specific fragility, where masking a single patch reduces accuracy by $18.7\% \pm 4.1\%$ on average. Quantitatively, using causal inference tool TDE (VanderWeele, 2013) to quantify each patch's impact—measured as the classification logit difference with and without that patch—we find that naively trained detectors produce skewed distributions: a few patches show high TDE values, while most patches exhibit significantly lower contributions. This suggests that most patches remain underutilized, despite also containing generative artifacts. Moreover, *detection methods with more uniform TDE distributions exhibit stronger generalizability*; for instance, DRCT, with more high-TDE patches, performs substantially better than UnivFD. We attribute such *Few Patch Bias* to the propensity of detectors as *Lazy Learner* (Hermann et al., 2024; Zhang et al., 2021; Wang et al., 2022; Zhao et al., 2024; Ghosh et al., 2023; Tang et al., 2023; Sun et al., 2024; Yuan et al., 2024; Yan et al., 2024b). Specifically, AIGI detectors follow a curriculum-like learning pattern: *once easy-to-learn artifacts in certain patches minimize loss, the presence of these patches discourages exploration of broader regions.*

To address this challenge, we propose the principle: "All Patches Matter, More Patches Better", which prevents detectors from shortcutting to a few regions and instead encourages robust feature learning across the entire image. To operationalize this principle, we introduce the **Panoptic Patch Learning** (PPL) framework, which consists of two components: (1) *Randomized Patch Reconstruction*, which manually injects synthetic artifacts into randomly selected patches of real images via diffusion reconstruction, forcing the model to discriminate based on these chosen regions and discouraging over-reliance on specific patches; and (2) *Patch-wise Contrastive Learning*, which aligns the representations of real and synthetic patches, thereby enforcing consistent discriminative capability across all regions of the image. Fig. 1 illustrates the effectiveness of PPL. Our main contributions are threefold:

1. We formally propose the principle "All Patches Matter, More Patches Better", showing that exploiting distributed artifacts enhances AIGI detection.
2. We provide a detailed patch-wise analysis using TDE, revealing that Few-Patch Bias is pervasive in existing detectors.

3. Building on this principle, we design Panoptic Patch Learning and validate its effectiveness through extensive experiments.

2 Related Work

Existing AIGI detection methods can be broadly categorized into two types: *local* and *global* detection (Tan et al., 2024a). We summarize both lines of research below.

Local AIGI detection methods. Local approaches exploit localized information to distinguish AI-generated images from real ones, assuming that low-level feature differences exist between the two. These methods can be divided into *patch-wise* and *pixel-wise* detectors.

Patch-wise methods include: SSP (Chen et al., 2024b) achieves notable performance using only a single patch. Patchcraft (Zhong et al., 2024) separates processing of the simplest and most complex patches by entropy-based selection. (Zheng et al., 2024) employ a patch-based CNN leveraging all patches to avoid selective sampling and aggregate patch features. TextureCrop (Konstantinidou et al., 2025) partitions an image via sliding windows and selects high-frequency texture-rich regions. Despite these advances, patch-wise detectors often over-rely on a limited subset of patches, leading to information under-utilization. *Pixel-wise methods* include: NPR (Tan et al., 2024c) detects AIGIs by analyzing differences in neighboring pixel relationships. FreqNet (Tan et al., 2024b) and SAFE (Li et al., 2024) exploit high-frequency signals to capture localized patterns. However, pixel-wise methods are sensitive to small perturbations in pixel relationships, limiting their robustness.

Global AIGI detection methods. Global approaches leverage holistic image characteristics to distinguish AIGIs from real images, aiming to capture inconsistencies that may not be observable at the local level. CNNSpot (Wang et al., 2020) applies a CNN directly for detection, achieving strong in-distribution performance but suffering from poor cross-generator generalization. UnivFD (Ojha et al., 2023) improves robustness by adopting a CLIP visual encoder as a feature extractor. FatFormer (Liu et al., 2024) further adapts CLIP by introducing a frequency adapter. C2P-CLIP (Tan et al., 2024a) fine-tunes CLIP with carefully designed image–text pairs to embed the notions of "real" and "fake." DRCT (Chen et al., 2024a) strengthens UnivFD with a contrastive loss on hard cases. Nevertheless, global methods often overlook fine-grained forensic artifacts, which constrains their effectiveness.

3 Motivation

3.1 All Patches Matter, More Patches Better

The principle of *All Patches Matter* is supported by three key findings.

1. **Theory:** Because every patch of a synthetic image is itself generated, each inherently contains artifacts. Localized detection methods (Chen et al., 2024b; Zhong et al., 2024) demonstrate that cues within small regions can effectively discriminate real from synthetic content, underscoring that every patch carries discriminative signals.
2. **Visualization:** Fig. 2 illustrates distinct artifact patterns across patches, showing that each synthetic patch exhibits identifiable features distinguishing it from real patches. Moreover, the variability of these cues across patches highlights the considerable diversity of artifacts present in synthetic images.
3. **Experiments:** We further validated this principle by evaluating detectors on single randomly selected patches. By replicating one patch across the image to isolate its features, detectors still achieved 90% accuracy on the SDv1.4 subset of GenImage. This confirms that even a single patch contains sufficient information for reliable discrimination.

Together, these findings demonstrate that artifacts in synthetic images are both pervasive and diverse. Detectors can exploit these patch-level cues, motivating the principle of *More Patches Better*: leveraging more patches enhances robustness and generalization by capturing complementary artifact patterns. However, our observations reveal that existing detectors donot align with this principle.

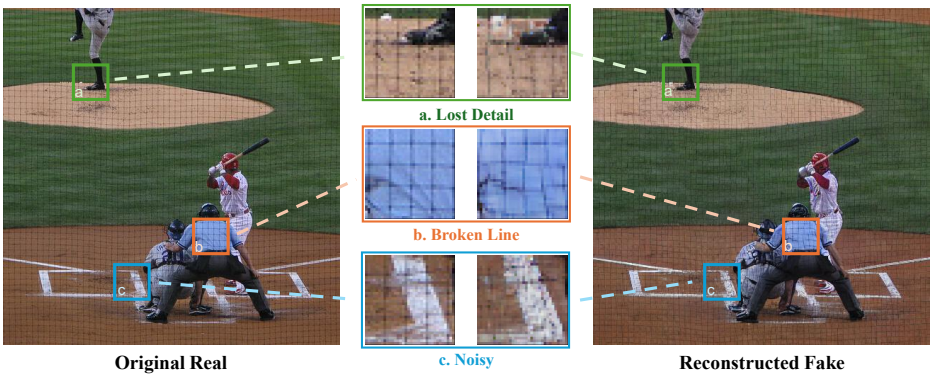

Figure 2: Visual evidence of patch-wise artifacts. We observe diverse traces—such as broken lines, unnatural noise, and boundary detail loss—showing that multiple regions of synthetic images contain cues. This observation underscores the importance of *leveraging more patches to enhance recognition of diverse artifacts*. Images are sourced from MSCOCO (Lin et al., 2014).

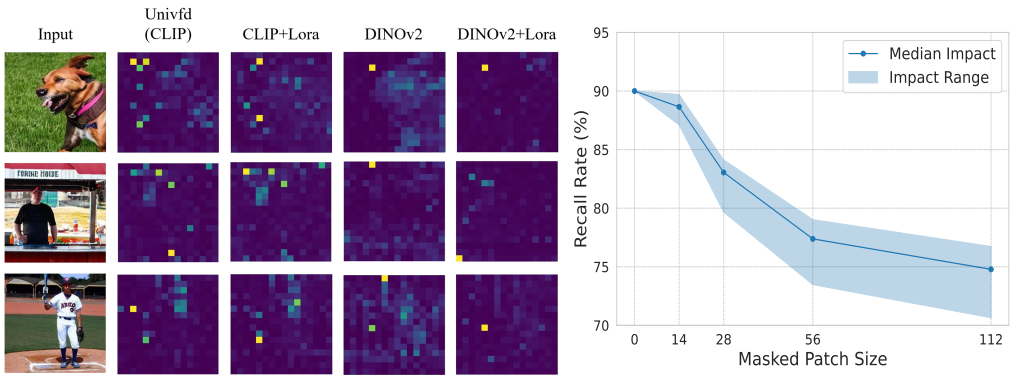

(a) Visualization of Attention Maps.

(b) Impact of Patch Removal on Recall Rate.

Figure 3: **(a)** Attention maps reveal the *few-patch bias* of naively trained detectors, where attention concentrates on a small number of dominant patches, reflecting over-reliance on limited regions. **(b)** Recall degradation occurs when single patches of varying sizes are occluded, showing that detectors are overly sensitive to corruption in specific regions and suffer notable performance drops.

3.2 Few-Patch Bias

Observations. Our empirical observations indicate that existing detectors often overly rely on a limited number of patches. Our experiments reveal that existing detectors tend to over-rely on a limited set of patches. Fig. 3(a) shows attention maps from naively trained ViTs, where attention weights concentrate on only a few regions. This phenomenon persists even when changing the backbone or applying LoRA, suggesting a model-agnostic bias. To further validate this observation, we systematically mask patches of varying sizes and measured the corresponding recall rate degradation. Fig. 3(b) illustrates the performance of UnivFD under patch occlusion. Masking a single patch leads to a substantial drop in accuracy, and the impact varies across different patches, confirming that detectors are disproportionately sensitive to specific regions.

Quantitative analysis. Building on the above observations, we employ the Total Direct Effect (TDE) to quantify the impact of each patch. Conceptually, if both $X \to Y$ and $Z \to Y$, then the outcome Y results from the combined influence of X and Z. The TDE measures the contribution of X by comparing outcomes with and without its effect while keeping other factors fixed.

For an image, the TDE of the patch at row i, column j is defined as:

$$TDE := \delta_I - \delta_{I-(i,j)}, \quad \delta := \text{logit}_{synth} - \text{logit}_{real}, \tag{1}$$

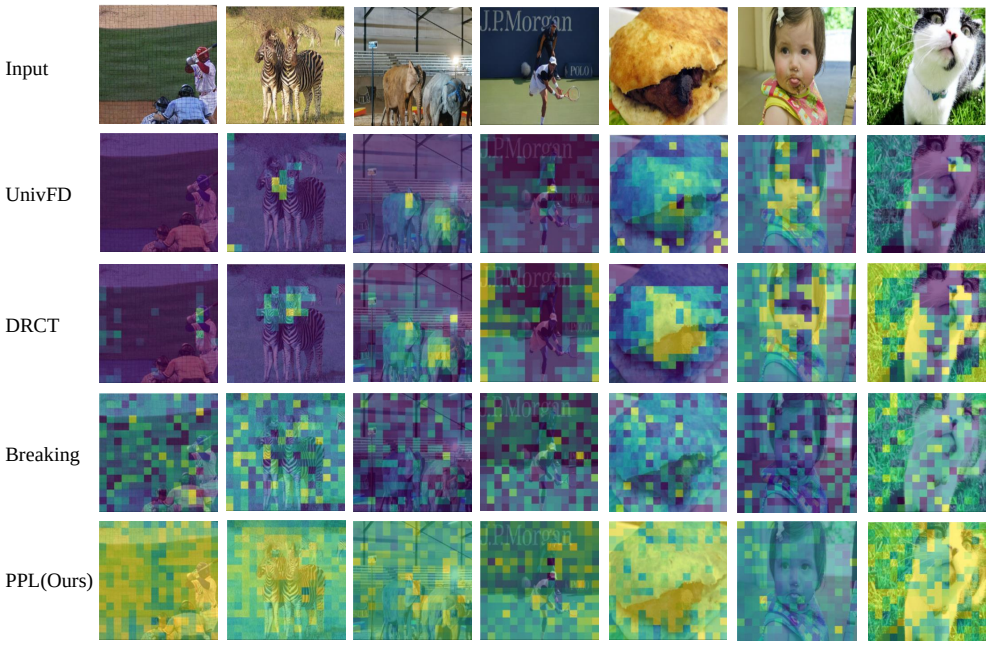

Figure 4: TDE heatmap of existing methods on generated images selected from the DRCT-2M dataset (Chen et al., 2024a). A broader and more uniform highlighted region indicates a greater number of patches contributing to determining a fake image.

where I denotes the original image and $I - (i, j)$ the image with the (i, j)-th patch masked (implemented by setting the patch values to zero). By computing the TDE for each patch, we quantify its relative contribution to the synthetic classification decision.

Fig. 4 presents TDE heatmaps. From top to bottom, the number of active patches increases and the TDE distributions become more uniform. Stronger detectors consistently activate a broader set of patches. These visualizations highlight the prevailing bias toward a few dominant patches with disproportionately high TDE, motivating us to mitigate few-patch reliance.

4 METHODOLOGY

Panoptic Patch Learning is a comprehensive framework based on the principles of "All Patches Matter" and "More Patches Better," achieved through innovative data and learning strategies, as illustrated in Fig. 5. Specifically, the data strategy, Randomized Patch Reconstruction (RPR), discourages the model from over-relying on any specific patches, thereby enhancing its recognition capability for various artifacts across *more patches*. Following this, the learning strategy, Patch-wise Contrastive Learning (PCL), ensures that *all patches*, both frequently attended and underutilized, are brought closer in the feature space, thereby uniformizing the impact of all patches.

Randomized Patch Reconstruction encourages "More Patches Better". The RPR process is carried out by performing diffusion reconstruction on randomly selected patches with a specified proportion, injecting synthetic cues into specific regions of the image while maintaining the overall semantics of the image (as the reconstructed image closely resembles the original image). In practice, RPR is implemented by first applying diffusion reconstruction to the entire image to obtain a reconstructed version. Then, the selected patches in the original image are replaced with their reconstructed counterparts, resulting in a synthetic image where only specific regions contain synthetic artifacts. Here, we emphasize that we inject synthetic features via diffusion reconstruction rather than stitching a synthetic patch, in order to preserve the global semantics and integration of the produced image, and to prevent the model from overfitting to images with disconnected semantics. We use $r \in [0, 1.0]$ to denote the ratio of reconstructed patches relative to the whole image.

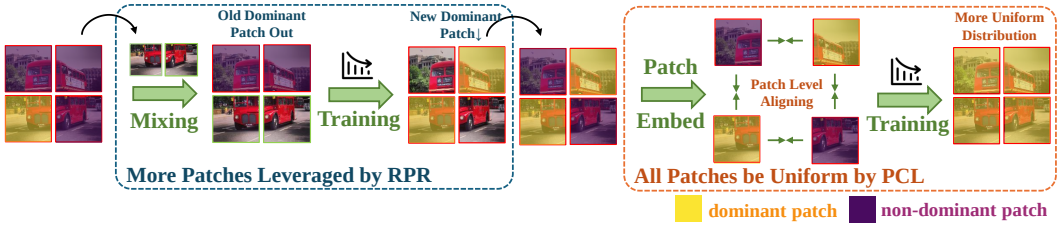

Figure 5: The Panoptic Patch Learning (PPL) framework embodies the principles of **All Patches Matter** and **More Patches Better** through two key components: Randomized Patch Reconstruction (RPR) and Patch-wise Contrastive Learning (PCL). During training, the model may excessively rely on **dominant patches**, neglecting others. RPR mitigates this by randomly replacing dominant patches with real ones, encouraging the model to detect artifacts in **non-dominant patches** and thereby expanding the coverage of dominant regions. PCL further promotes balanced patch utilization by aligning the embeddings of patches with the same labels. Together, RPR and PCL foster comprehensive and uniform exploitation of patches.

Algorithm 1 Patch-wise Contrastive Learning (PCL) Training Procedure

Input:

X – input image tensor after RPR, shape $[B, C, H, W]$
$label_{gt}$ – image-level ground-truth labels, shape $[B]$
$patch_{gt}$ – patch-level ground-truth labels, shape $[B, K]$
λ – weighting coefficient for contrastive loss

$img_{embedding}, patch_{embedding} \leftarrow ViT_{Encoder}(X)$ ▷ $img_{embedding}$: $[B, 1, D]$, $patch_{embedding}$: $[B, K, D]$
$y_{pred} \leftarrow \text{Linear}(img_{embedding})$ ▷ Image-level class logits, shape $[B, 2]$
$L_{ce} \leftarrow \text{BCELoss}(y_{pred}, label_{gt})$ ▷ Image-level classification loss
$L_{con} \leftarrow \text{ContrastiveLoss}(patch_{embedding}, patch_{gt})$ ▷ Patch-level contrastive loss
$L_{total} \leftarrow \lambda \cdot L_{con} + (1 - \lambda) \cdot L_{bce}$
L_{total}.backward()

Patch-wise Contrastive Learning emphasizes "All Patches Matter". PCL operationalizes the principle of "All Patches Matter" by aligning the embedding vectors of different patches, bringing patches with identical labels closer together while distancing those with different labels. We employ contrastive learning to cluster synthetic patches more closely within each batch, while maintaining a margin that separates synthetic and real patches. This approach ensures that if an image contains any dominant patch with easily learnable artifacts, the model improves its performance on the remaining patches, thus promoting the utilization of all patches. Specifically, for each batch, we utilize a margin-based contrastive loss (Hadsell et al., 2006):

$$\mathcal{L}_{con} = \sum_{i,j:\, i \neq j} \left[Y \cdot d^2 + (1 - Y) \cdot \max\left(0, \alpha - d^2\right) \right], \tag{2}$$

where i, j represent the indices of patch tokens within a batch. d measures the Euclidean distance between the patch embeddings. α defines a minimum distance threshold between negative sample pairs, thereby enhancing the model's ability to distinguish between similar and dissimilar pairs. Y indicates whether two patches share identical labels, thus pulling positive patch pairs closer and pushing negative patch pairs further apart. The overall loss function is a weighted combination of the cross-entropy loss and the patch-wise contrastive loss:

$$\mathcal{L}_{\text{total}} = \lambda \mathcal{L}_{\text{con}} + (1 - \lambda) \mathcal{L}_{\text{ce}}, \tag{3}$$

The practical implementation of PCL is shown in Alg. 1.

5 Experiments

Implementation details. We adopt CLIP (Radford et al., 2021) and DINOv2 (Oquab et al., 2023) two vision foundation model as backbones , and fine-tune them using LoRA. Unless otherwise

Table 1: Cross-model accuracy (Acc) on GenImage. All methods are trained on the SDv1.4 subset. Results are taken from C2P-CLIP (Tan et al., 2024a), except SAFE and Effort, which are reported in their original papers. For Breaking (Zheng et al., 2024), we re-implement the method because no GenImage results or checkpoints are publicly available. Our results are bolded when they achieve the highest accuracy among all methods.

Method	Ref	Midjourney	SDv1.4	SDv1.5	ADM	GLIDE	Wukong	VQDM	BigGAN	mAcc
ResNet-50 (He et al., 2016)	CVPR2016	54.9	99.9	99.7	53.5	61.9	98.2	56.6	52.0	72.1 ± 22.6
DeiT-S (Touvron et al., 2021)	ICML2021	55.6	99.9	99.8	49.8	58.1	98.9	56.9	53.5	71.6 ± 23.2
Swin-T (Liu et al., 2021)	ICCV2021	62.1	99.9	99.8	49.8	67.6	99.1	62.3	57.6	74.8 ± 21.1
CNNSpot (Wang et al., 2020)	CVPR2020	52.8	96.3	95.9	50.1	39.8	78.6	53.4	46.8	64.2 ± 22.6
Spec (Zhang et al., 2019)	WIFS2019	52.0	99.4	99.2	49.7	49.8	94.8	55.6	49.8	68.8 ± 24.1
F3Net (Qian et al., 2020)	ECCV2020	50.1	99.9	99.9	49.9	50.0	99.9	49.9	49.9	68.7 ± 25.8
GramNet (Liu et al., 2020)	CVPR2020	54.2	99.2	99.1	50.3	54.6	98.9	50.8	51.7	69.9 ± 24.2
UnivFD (Ojha et al., 2023)	CVPR2023	93.9	96.4	96.2	71.9	85.4	94.3	81.6	90.5	88.8 ± 8.6
NPR (Tan et al., 2024c)	CVPR2024	81.0	98.2	97.9	76.9	89.8	96.9	84.1	84.2	88.6 ± 8.3
FreqNet (Tan et al., 2024b)	AAAI2024	89.6	98.8	98.6	66.8	86.5	97.3	75.8	81.4	86.8 ± 11.6
FatFormer (Liu et al., 2024)	CVPR2024	92.7	100.0	99.9	75.9	88.0	99.9	98.8	55.8	88.9 ± 15.7
DRCT (Chen et al., 2024a)	ICML2024	91.5	95.0	94.4	79.4	89.1	94.6	90.0	81.6	89.4 ± 5.9
Effort (Yan et al., 2024b)	ICML2025	82.4	99.8	99.8	78.7	93.3	97.4	91.7	77.6	91.1 ± 11.8
Breaking (Zheng et al., 2024)	NIPS2024	83.9	98.9	93.0	99.1	97.7	85.4	92.7	90.5	92.7 ± 5.8
SAFE (Li et al., 2024)	KDD2025	95.3	99.4	99.3	82.1	96.3	98.2	96.3	97.8	95.6 ± 5.6
C2P-CLIP (Tan et al., 2024a)	AAAI2025	88.2	90.9	97.9	96.4	99.0	98.8	96.5	98.7	95.8 ± 4.0
Ours/DINOv2		90.4	98.2	97.7	91.8	96.3	98.0	97.7	96.2	**95.9** ± 3.0
Ours/CLIP		94.8	98.5	98.3	94.7	96.1	98.6	98.5	98.0	**97.2** ± 1.7

Table 2: Cross-model accuracy (Acc) on DRCT-2M. All methods are trained on the SDv1.4 subset. Results of other methods are taken from DRCT (Chen et al., 2024a).

Method	SD Variants					Turbo Variants			LCM Variants		ControlNet Variants			DR Variants			mAcc
	LDM	SDv1.4	SDv1.5	SDv2	SDXL	SDXL-Refiner	SD-Turbo	SDXL-Turbo	LCM-SDv1.5	LCM-SDXL	SDv1-Ctrl	SDv2-Ctrl	SDXL-Ctrl	SDv1-DR	SDv2-DR	SDX-L DR	
CNNSpot (Wang et al., 2020)	99.87	99.91	99.90	97.55	66.25	86.55	86.15	72.42	98.26	61.72	97.96	85.89	82.84	60.93	51.41	50.28	81.12 ± 17.6
F3Net (Qian et al., 2020)	99.85	99.78	99.79	88.66	55.85	87.37	68.29	63.66	97.39	54.98	97.98	72.39	81.99	65.42	50.39	50.27	77.13 ± 18.1
CLIP/RN50 (Radford et al., 2021)	99.00	99.99	99.96	94.61	62.08	91.43	83.57	64.40	98.97	57.43	99.74	80.69	82.03	65.83	50.67	50.47	80.05 ± 18.3
GramNet (Liu et al., 2020)	99.40	99.01	98.84	95.30	62.63	80.68	71.19	69.32	93.05	57.02	89.97	75.55	82.68	51.23	50.01	50.08	76.62 ± 17.0
De-fake (Sha et al., 2023)	92.10	99.53	99.51	89.65	64.02	69.24	92.00	93.93	99.13	70.89	58.98	62.34	66.66	50.12	50.16	50.00	75.52 ± 18.4
Conv-B (Liu et al., 2022)	99.97	100.0	99.97	95.84	64.44	82.00	80.82	60.75	99.27	62.33	99.80	83.40	73.28	61.65	51.79	50.41	79.11 ± 18.3
UnivFD (Ojha et al., 2023)	98.30	96.22	96.33	93.83	91.01	93.91	86.38	85.92	90.44	88.99	90.41	81.06	89.06	51.96	51.03	50.46	83.46 ± 17.0
DRCT (Chen et al., 2024a)	94.45	94.35	94.24	95.05	95.61	95.38	94.81	94.48	91.66	95.54	93.86	93.48	93.54	84.34	83.20	67.61	91.35 ± 4.7
Ours/DINOv2	99.55	99.55	99.55	99.54	99.55	94.70	99.53	99.23	99.31	99.55	99.54	99.55	99.39	99.48	99.55	97.42	99.06 ± 0.1
Ours/CLIP	99.70	99.70	99.69	99.67	99.71	99.40	99.48	99.40	99.62	99.70	99.68	99.64	99.51	99.61	99.67	97.80	**99.50** ± 0.1

specified, in our proposed Panoptic Patch Learning (PPL), image reconstruction is performed with SDv1.4 inpainting at a generation strength of $s = 0.25$. The inpainting pipeline uses $step = 50$ and guidance scale 7.5. During training, images are randomly cropped to 224×224, while at test time they are center-cropped to the same resolution. For the randomized patch reconstruction module, the reconstruction patch size is set to 14×14, consistent with the patch size of ViT. Each fake image in the original training set has a probability of $p_{rpr} = 0.9$ of being replaced with a RPR image, where $r_{rpr} = 50\%$ of patches from a real image are randomly selected to do diffusion reconstruction. For patch-wise contrastive learning, the weight of the contrastive loss is set to $\lambda = 0.3$, with a margin parameter $\alpha = 1.0$.

Peer methods. The compared methods involve ResNet-50 (He et al., 2016), Conv-B (Liu et al., 2022), Swin-T (Liu et al., 2021), CNNSpot (Wang et al., 2020), F3Net (Li et al., 2021), SAFE (Qian et al., 2020), UnivFD (Ojha et al., 2023), FatFormer (Liu et al., 2024), DRCT (Chen et al., 2024a), C2P-CLIP (Tan et al., 2024a), Effort (Yan et al., 2024b).

5.1 Comparison with other methods

Comparison on GenImage. Tab. 1 compares PPL with other methods on GenImage. We observe: (1) PPL consistently achieves higher accuracy across different backbones. (2) The standard deviation of PPL's accuracy is smaller, indicating improved stability in detecting diverse generative models.

Comparison on DRCT-2M. Tab. 2 reports results on DRCT-2M. The results indicate: (1) PPL consistently achieves SoTA with the lowest std, demonstrating both effectiveness and stability. (2) While DRCT shows relatively poor performance on SDXL-related subsets, PPL maintains a more balanced performance across diverse subsets, underscoring its robustness.

Table 3: Cross-dataset and cross-model accuracy (mAcc) on AIGCDetectionBenchmark. PPL is trained on the GenImage SDv1.4 subset due to its reliance on diffusion-based reconstruction. Baseline methods are trained on ProGAN data provided by AIGCDetectionBenchmark, which is more in-distribution with the test set, thereby giving them an inherent advantage under this setting. Baseline results are taken from AIDE (Yan et al., 2024a).

Method	ProGAN	StyleGAN	BigGAN	CycleGAN	StarGAN	GauGAN	StyleGAN2	WFR	ADM	Glide	Midjourney	SD v1.4	SD v1.5	VQDM	Wukong	DALLE2	mAcc
CNNSpot	100.00	90.17	71.17	87.62	94.60	81.42	86.91	91.65	60.39	58.07	51.39	50.57	50.53	56.46	51.03	50.45	70.78 ± 18.30
FreDect	99.36	78.02	81.97	78.77	94.62	80.57	66.19	50.75	63.42	54.13	45.87	38.79	39.21	77.80	40.30	34.70	64.03 ± 20.41
Fusing	100.00	85.20	77.40	87.00	97.00	77.00	83.30	66.80	49.00	57.20	52.20	51.00	51.40	55.10	51.70	52.80	68.38 ± 17.46
LNP	99.67	91.75	77.75	84.10	99.92	75.39	94.64	70.85	84.73	80.52	65.55	85.55	85.67	74.46	82.06	88.75	83.84 ± 9.46
LGrad	99.83	91.08	85.62	86.94	99.27	78.46	85.32	55.70	67.15	66.11	65.35	63.02	63.67	72.99	59.55	65.45	75.34 ± 13.8
UnivFD	99.81	84.93	95.08	98.33	95.75	99.47	74.96	86.90	66.87	62.46	56.13	63.66	63.49	85.31	70.93	50.75	78.43 ± 16.19
DIRE-G	95.19	83.03	70.12	74.19	95.47	67.79	75.31	58.05	75.78	71.75	58.01	49.74	49.83	53.68	54.46	66.48	68.68 ± 14.00
DIRE-D	52.75	51.31	49.70	49.58	46.72	51.23	51.72	53.30	98.25	92.42	89.45	91.24	91.63	91.90	90.90	92.45	71.53 ± 20.86
PatchCraft	100.00	92.77	95.80	70.17	99.97	71.58	89.55	85.80	82.17	83.79	90.12	95.38	95.30	88.91	91.07	96.60	89.31 ± 8.61
AIDE	99.99	99.64	83.95	98.48	99.91	73.25	98.00	94.20	93.43	95.09	77.20	93.01	92.85	95.16	93.55	96.60	92.77 ± 7.66
NPR	99.79	97.70	84.35	96.10	99.35	82.50	98.38	65.80	69.69	78.36	77.85	78.63	78.89	78.13	76.11	64.90	82.91 ± 11.54
Ours/DINOv2	96.94	94.27	94.73	89.44	89.99	93.99	89.44	95.00	91.02	97.84	85.00	99.43	99.03	99.17	99.26	96.05	**94.41** ± 4.20
Ours/CLIP	89.12	89.94	83.57	97.16	97.12	75.29	89.17	95.20	94.67	96.05	94.78	98.49	98.19	98.53	98.61	97.90	**93.36** ± 6.31

Table 4: Cross-dataset and cross-model accuracy (mAcc) on the UniversalFakeDetect. PPL is trained on the SDv1.4 subset of GenImage, while other methods are trained on GAN. Baseline results are taken from C2P-CLIP (Tan et al., 2024a).

Methods	Ref	GAN						Guided	LDM			GLIDE			DALLE	mAcc
		Pro-GAN	Cycle-GAN	Big-GAN	Style-GAN	Gau-GAN	Star-GAN		200 steps	200 w/cfg	100 steps	100 27	50 27	100 10		
CNN-Spot	CVPR2020	99.99	85.20	70.20	85.70	78.95	91.70	60.07	54.03	54.96	54.14	60.78	63.80	65.66	55.58	70.05 ± 14.90
Patchfor	ECCV2020	75.03	68.97	68.47	79.16	64.23	63.94	67.41	76.50	76.10	75.77	74.81	73.28	68.52	67.91	71.44 ± 4.73
Co-occurence	Elect. Imag.	97.70	63.15	53.75	92.50	51.10	54.70	60.50	70.70	70.55	71.00	70.25	69.60	69.90	67.55	68.78 ± 12.68
Freq-spec	WIFS2019	49.90	99.90	50.50	49.90	50.30	99.70	50.90	50.40	50.40	50.30	51.70	51.40	50.40	50.00	57.55 ± 17.25
F3Net	ECCV2020	99.38	76.38	65.33	92.56	58.10	100.00	69.20	68.15	75.35	68.80	81.65	83.25	83.05	66.30	77.68 ± 12.47
UnivFD	CVPR2023	100.00	98.50	94.50	82.00	99.50	97.00	70.03	94.19	73.76	94.36	79.07	79.85	78.14	86.78	87.69 ± 9.97
LGrad	CVPR2023	99.84	85.39	82.88	94.83	72.45	99.62	77.50	94.20	95.85	94.80	87.40	90.70	89.55	88.35	89.53 ± 7.70
FreqNet	AAAI2024	97.90	95.84	90.45	97.55	90.24	93.41	86.70	84.55	99.58	65.56	85.69	97.40	88.15	59.06	88.01 ± 11.56
NPR	CVPR2024	99.84	95.00	87.55	96.23	86.57	99.75	84.55	97.65	98.00	98.20	96.25	97.15	97.35	87.15	94.37 ± 5.19
FatFormer	CVPR2024	99.89	99.32	99.50	97.15	99.41	99.75	76.00	98.60	94.90	98.65	94.35	94.65	94.20	98.75	**96.08** ± 5.95
C2P-CLIP	AAAI2025	99.98	97.31	99.12	96.44	99.17	99.60	69.10	99.25	97.25	99.30	95.25	95.25	96.10	98.55	95.83 ± 7.57
Ours/DINOv2		96.94	89.44	94.73	94.27	93.99	89.99	92.30	99.40	99.40	99.40	98.35	98.60	98.50	99.40	96.05 ± 3.58
Ours/CLIP		89.12	97.16	83.57	89.94	75.29	97.12	94.55	98.80	98.80	98.80	96.90	97.40	97.65	98.80	93.85 ± 6.78

Table 5: Cross-dataset accuracy (Acc) on the in-the-wild dataset Chameleon. Results of other methods are directly taken from AIDE (Yan et al., 2024a). For each training dataset, the first row reports the overall **Acc** on the Chameleon test set, while the second row presents **Acc** separately for **fake images** and **real images** for detailed analysis.

Training Dataset	CNNSpot	FreDect	Fusing	UnivFD	DIRE	PatchCraft	NPR	AIDE	Ours/CLIP	Ours/DINOv2
SD v1.4	60.11	56.86	57.07	55.62	59.71	56.32	58.13	62.60	<u>63.94</u>	**66.63**
	8.86/98.63	1.37/98.57	0.00/99.96	17.65/93.50	11.86/95.67	3.07/96.35	2.43/100.00	20.33/94.38	17.27/99.01	64.65/68.12
All GenImage	60.89	57.22	57.09	60.42	57.83	55.70	57.81	65.77	<u>69.33</u>	**72.07**
	9.86/99.25	0.89/99.55	0.02/99.98	85.52/41.56	2.09/99.73	1.39/96.52	1.68/100.00	26.80/95.06	38.93/92.18	49.68/88.99

Comparison on AIGCDetectBenchmark and UniversalFakeDetect. Tab. 3 and Tab. 4 present results on AIGCDetectBenchmark (Zhong et al., 2024) and UniversalFakeDetect (Ojha et al., 2023), respectively. The results of baseline methods are taken from (Yan et al., 2024a) and (Tan et al., 2024a). We observe that PPL, when trained solely on diffusion-generated data, generalizes effectively to detecting GAN-generated images—even surpassing baseline methods trained directly on GAN data—highlighting PPL's strong generalization capability.

Comparison on the in-the-wild dataset Chameleon. Tab. 5 reports results on Chameleon, a challenging dataset comprising diverse images collected from online websites. We observe that most existing methods only marginally exceed the accuracy of random guessing (50%). In contrast, PPL achieves 70% accuracy on Chameleon, demonstrating strong generalization on real-world data.

5.2 Robustness Studies

We conduct robustness experiments on GenImage to evaluate the reliability of our method under common image corruptions. As shown in Fig. 6, both CLIP and DINOv2 backbones sustain high accuracy even under severe JPEG compression and strong Gaussian blur, demonstrating the robustness of our approach.

5.3 Ablation Study

Ablation on the hyperparameters. Fig. 7 reports the influence of key hyperparameters in PPL. The results suggest four main observations: (1) PPL achieves peak accuracy at $\lambda = 0.3$. (2) PPL is

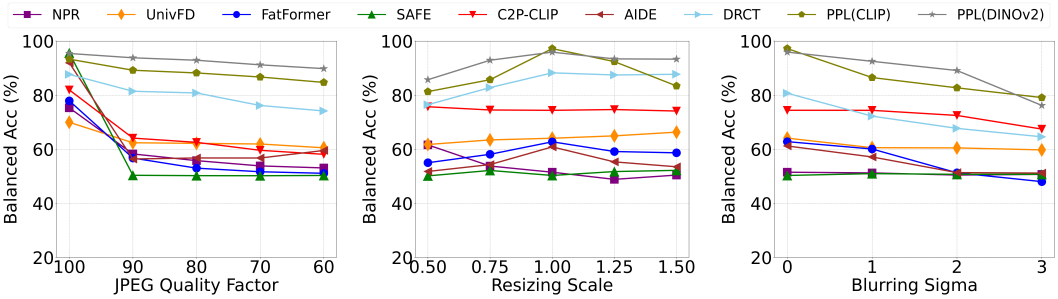

Figure 6: Robustness to image corruptions on GenImage Dataset. Performance is evaluated under JPEG compression (quality factor $Q \in \{100, 90, 80, 70, 60\}$), Gaussian blur (standard deviation $\sigma \in \{0.0, 1.0, 2.0, 3.0\}$), and resizing (scaling factor $S \in \{0.5, 0.75, 1.0, 1.25, 1.5\}$).

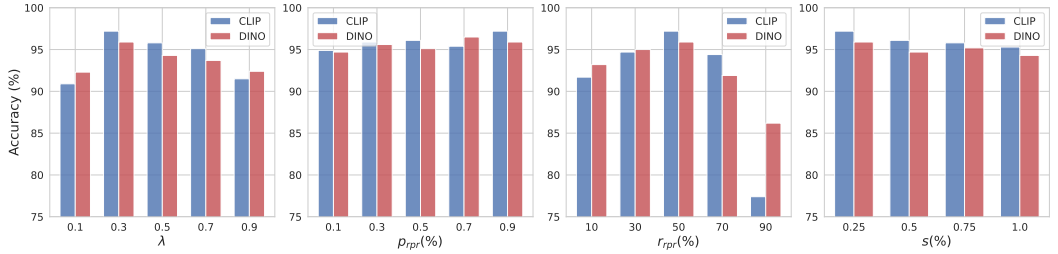

Figure 7: Ablation study on hyperparameters: λ representing the weight of contrastive loss. p_{rpr} representing the probability of replacing the fake images with RPR images during training. r_{rpr} representing the ratio of reconstructed patches, and s representing the strength of reconstruction.

relatively robust to p_{rpr}, the probability of replacing fake images with RPR images during training. (3) PPL is sensitive to the patch reconstruction ratio r_{rpr}, where accuracy degrades at excessively high ratios, with the best performance obtained around $r_{rpr} = 50\%$. (4) Smaller reconstruction strength s not only improves accuracy but also reduces computational cost, making it preferable in practice.

Ablation on the impact of each module. Fig. 8 highlights the contributions of Randomized Patch Reconstruction (RPR) and Patch-wise Contrastive Learning (PCL). We compare two strategies for injecting synthetic artifacts into real images: (1) diffusion-based reconstruction (blue), and (2) random patch replacement from synthetic images (red). The results show that reconstruction serves as a more effective mechanism for introducing synthetic cues to guide the model. While either RPR or PCL alone enhances performance, their combination yields markedly stronger improvements. Additional ablation studies are provided in the Appendix due to space constraints.

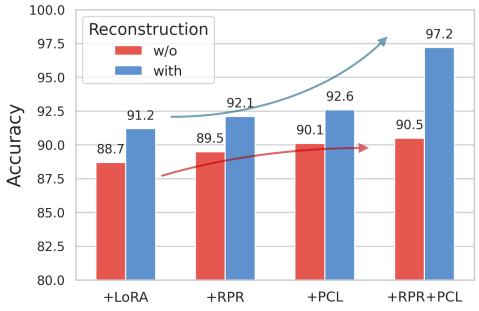

Figure 8: Ablation study on each module.

6 Conclusion

Our work is based on the nature of the AIGI detection problem, which can be concluded as "All Patches Matter, More Patches Better." However, our observations indicate that existing detectors are unable to fully take advantage of all patches in an AI-generated image. To address this issue, we propose a randomized patch reconstruction augmentation combined with patch-wise contrastive learning strategy. This approach effectively prevents the model from becoming a lazy learner and enhances the utilization of every patch. We achieve state-of-the-art performance on several well-known academic datasets across various benchmark datasets. The outstanding performance achieved in both settings supports our findings and proves the efficacy of the proposed learning framework.

REFERENCES

Baoying Chen, Jishen Zeng, Jianquan Yang, and Rui Yang. Drct: Diffusion reconstruction contrastive training towards universal detection of diffusion generated images. In *Forty-first International Conference on Machine Learning*, 2024a.

Jiaxuan Chen, Jieteng Yao, and Li Niu. A single simple patch is all you need for ai-generated image detection. *arXiv preprint arXiv:2402.01123*, 2024b.

Davide Cozzolino, Giovanni Poggi, Matthias Nießner, and Luisa Verdoliva. Zero-shot detection of ai-generated images. In *European Conference on Computer Vision*, pp. 54–72. Springer, 2024.

Shantanu Ghosh, Ke Yu, Forough Arabshahi, and Kayhan Batmanghelich. Tackling shortcut learning in deep neural networks: An iterative approach with interpretable models. *arXiv preprint arXiv:2302.10289*, 2023.

Ian J Goodfellow et al. Generative adversarial nets. In *Advances in Neural Information Processing Systems*, 2014.

Raia Hadsell, Sumit Chopra, and Yann LeCun. Dimensionality reduction by learning an invariant mapping. In *2006 IEEE computer society conference on computer vision and pattern recognition (CVPR'06)*, volume 2, pp. 1735–1742. IEEE, 2006.

Kaiming He et al. Deep residual learning for image recognition. In *Proceedings of the IEEE Conference on Computer Vision and Pattern Recognition*, pp. 770–778, 2016.

Zhiyuan He, Pin-Yu Chen, and Tsung-Yi Ho. Rigid: A training-free and model-agnostic framework for robust ai-generated image detection. *arXiv preprint arXiv:2405.20112*, 2024.

Katherine Hermann, Hossein Mobahi, Thomas FEL, and Michael Curtis Mozer. On the foundations of shortcut learning. In *The Twelfth International Conference on Learning Representations*, 2024.

Jonathan Ho et al. Denoising diffusion probabilistic models. *Advances in Neural Information Processing Systems*, 33:6840–6851, 2020.

Tero Karras et al. Progressive growing of gans for improved quality, stability, and variation. In *International Conference on Learning Representations*, 2018.

Tero Karras et al. A style-based generator architecture for generative adversarial networks. In *Proceedings of the IEEE/CVF Conference on Computer Vision and Pattern Recognition*, pp. 4401–4410, 2019.

Despina Konstantinidou, Christos Koutlis, and Symeon Papadopoulos. Texturecrop: Enhancing synthetic image detection through texture-based cropping. In *Proceedings of the Winter Conference on Applications of Computer Vision*, pp. 1459–1468, 2025.

Jiaming Li et al. Frequency-aware discriminative feature learning supervised by single-center loss for face forgery detection. In *Proceedings of the IEEE/CVF Conference on Computer Vision and Pattern Recognition*, pp. 6458–6467, 2021.

Ouxiang Li, Jiayin Cai, Yanbin Hao, Xiaolong Jiang, Yao Hu, and Fuli Feng. Improving synthetic image detection towards generalization: An image transformation perspective. *arXiv preprint arXiv:2408.06741*, 2024.

Tsung-Yi Lin, Michael Maire, Serge Belongie, James Hays, Pietro Perona, Deva Ramanan, Piotr Dollár, and C Lawrence Zitnick. Microsoft coco: Common objects in context. In *European conference on computer vision*, pp. 740–755. Springer, 2014.

Huan Liu, Zichang Tan, Chuangchuang Tan, Yunchao Wei, Jingdong Wang, and Yao Zhao. Forgery-aware adaptive transformer for generalizable synthetic image detection. In *Proceedings of the IEEE/CVF Conference on Computer Vision and Pattern Recognition*, pp. 10770–10780, 2024.

Ze Liu, Yutong Lin, Yue Cao, Han Hu, Yixuan Wei, Zheng Zhang, Stephen Lin, and Baining Guo. Swin transformer: Hierarchical vision transformer using shifted windows. In *Proceedings of the IEEE/CVF International Conference on Computer Vision*, pp. 10012–10022, 2021.

Zhengzhe Liu et al. Global texture enhancement for fake face detection in the wild. In *Proceedings of the IEEE/CVF Conference on Computer Vision and Pattern Recognition*, pp. 8060–8069, 2020.

Zhuang Liu, Hanzi Mao, Chao-Yuan Wu, Christoph Feichtenhofer, Trevor Darrell, and Saining Xie. A convnet for the 2020s. In *Proceedings of the IEEE/CVF conference on computer vision and pattern recognition*, pp. 11976–11986, 2022.

Utkarsh Ojha et al. Towards universal fake image detectors that generalize across generative models. In *Proceedings of the IEEE/CVF Conference on Computer Vision and Pattern Recognition*, pp. 24480–24489, 2023.

Maxime Oquab, Timothée Darcet, Théo Moutakanni, Huy Vo, Marc Szafraniec, Vasil Khalidov, Pierre Fernandez, Daniel Haziza, Francisco Massa, Alaaeldin El-Nouby, et al. Dinov2: Learning robust visual features without supervision. *arXiv preprint arXiv:2304.07193*, 2023.

Yuyang Qian et al. Thinking in frequency: Face forgery detection by mining frequency-aware clues. In *European Conference on Computer Vision*, pp. 86–103. Springer, 2020.

Alec Radford et al. Learning transferable visual models from natural language supervision. In *International Conference on Machine Learning*, pp. 8748–8763. PMLR, 2021.

Aditya Ramesh, Mikhail Pavlov, Gabriel Goh, Scott Gray, Chelsea Voss, Alec Radford, Mark Chen, and Ilya Sutskever. Zero-shot text-to-image generation. In *Proceedings of the 38th International Conference on Machine Learning*, 2021.

Robin Rombach et al. High-resolution image synthesis with latent diffusion models. In *Proceedings of the IEEE/CVF Conference on Computer Vision and Pattern Recognition*, pp. 10684–10695, 2022.

Zeyang Sha, Zheng Li, Ning Yu, and Yang Zhang. De-fake: Detection and attribution of fake images generated by text-to-image generation models. In *Proceedings of the 2023 ACM SIGSAC conference on computer and communications security*, pp. 3418–3432, 2023.

Zechen Sun, Yisheng Xiao, Juntao Li, Yixin Ji, Wenliang Chen, and Min Zhang. Exploring and mitigating shortcut learning for generative large language models. In *Proceedings of the 2024 Joint International Conference on Computational Linguistics, Language Resources and Evaluation (LREC-COLING 2024)*, pp. 6883–6893, 2024.

Chuangchuang Tan, Renshuai Tao, Huan Liu, Guanghua Gu, Baoyuan Wu, Yao Zhao, and Yunchao Wei. C2p-clip: Injecting category common prompt in clip to enhance generalization in deepfake detection. In *Proceedings of the AAAI Conference on Artificial Intelligence*, 2024a.

Chuangchuang Tan, Yao Zhao, Shikui Wei, Guanghua Gu, Ping Liu, and Yunchao Wei. Frequency-aware deepfake detection: Improving generalizability through frequency space domain learning. In *Proceedings of the AAAI Conference on Artificial Intelligence*, volume 38, pp. 5052–5060, 2024b.

Chuangchuang Tan, Yao Zhao, Shikui Wei, Guanghua Gu, Ping Liu, and Yunchao Wei. Rethinking the up-sampling operations in cnn-based generative network for generalizable deepfake detection. In *Proceedings of the IEEE/CVF Conference on Computer Vision and Pattern Recognition*, pp. 28130–28139, 2024c.

Ruixiang Tang, Dehan Kong, Longtao Huang, and Hui Xue. Large language models can be lazy learners: Analyze shortcuts in in-context learning. *arXiv preprint arXiv:2305.17256*, 2023.

Hugo Touvron, Matthieu Cord, Matthijs Douze, Francisco Massa, Alexandre Sablayrolles, and Hervé Jégou. Training data-efficient image transformers & distillation through attention. In *International Conference on Machine Learning*, pp. 10347–10357. PMLR, 2021.

Tyler J VanderWeele. A three-way decomposition of a total effect into direct, indirect, and interactive effects. *Epidemiology*, 2013.

Sheng-Yu Wang et al. Cnn-generated images are surprisingly easy to spot... for now. In *Proceedings of the IEEE/CVF Conference on Computer Vision and Pattern Recognition*, pp. 8695–8704, 2020.

Shunxin Wang, Raymond Veldhuis, Christoph Brune, and Nicola Strisciuglio. Frequency shortcut learning in neural networks. In *NeurIPS 2022 Workshop on Distribution Shifts: Connecting Methods and Applications*, 2022.

Shilin Yan, Ouxiang Li, Jiayin Cai, Yanbin Hao, Xiaolong Jiang, Yao Hu, and Weidi Xie. A sanity check for ai-generated image detection. *arXiv preprint arXiv:2406.19435*, 2024a.

Zhiyuan Yan, Jiangming Wang, Zhendong Wang, Peng Jin, Ke-Yue Zhang, Shen Chen, Taiping Yao, Shouhong Ding, Baoyuan Wu, and Li Yuan. Effort: Efficient orthogonal modeling for generalizable ai-generated image detection. *arXiv preprint arXiv:2411.15633*, 2024b.

Zhiyuan Yan, Taiping Yao, Shen Chen, Yandan Zhao, Xinghe Fu, Junwei Zhu, Donghao Luo, Chengjie Wang, Shouhong Ding, Yunsheng Wu, et al. Df40: Toward next-generation deepfake detection. *arXiv preprint arXiv:2406.13495*, 2024c.

Zhiyuan Yan, Junyan Ye, Weijia Li, Zilong Huang, Shenghai Yuan, Xiangyang He, Kaiqing Lin, Jun He, Conghui He, and Li Yuan. Gpt-imgeval: A comprehensive benchmark for diagnosing gpt4o in image generation. *arXiv preprint arXiv:2504.02782*, 2025.

Yu Yuan, Lili Zhao, Kai Zhang, Guangting Zheng, and Qi Liu. Do llms overcome shortcut learning? an evaluation of shortcut challenges in large language models. *arXiv preprint arXiv:2410.13343*, 2024.

Tianyu Zhang, Weiqing Min, Jiahao Yang, Tao Liu, Shuqiang Jiang, and Yong Rui. What if we could not see? counterfactual analysis for egocentric action anticipation. In *IJCAI*, pp. 1316–1322, 2021.

Xu Zhang et al. Detecting and simulating artifacts in gan fake images. In *2019 IEEE International Workshop on Information Forensics and Security (WIFS)*, pp. 1–6. IEEE, 2019.

Yabo Zhang, Yuxiang Wei, Dongsheng Jiang, Xiaopeng Zhang, Wangmeng Zuo, and Qi Tian. Controlvideo: Training-free controllable text-to-video generation. *arXiv preprint arXiv:2305.13077*, 2023.

Lili Zhao, Qi Liu, Linan Yue, Wei Chen, Liyi Chen, Ruijun Sun, and Chao Song. Comi: Correct and mitigate shortcut learning behavior in deep neural networks. In *Proceedings of the 47th International ACM SIGIR Conference on Research and Development in Information Retrieval*, pp. 218–228, 2024.

Chende Zheng, Chenhao Lin, Zhengyu Zhao, Hang Wang, Xu Guo, Shuai Liu, and Chao Shen. Breaking semantic artifacts for generalized ai-generated image detection. In *Advances in Neural Information Processing Systems*, 2024.

Nan Zhong, Yiran Xu, Sheng Li, Zhenxing Qian, and Xinpeng Zhang. Patchcraft: Exploring texture patch for efficient ai-generated image detection. *arXiv preprint arXiv:2311.12397*, pp. 1–18, 2024.

Mingjian Zhu, Hanting Chen, Qiangyu Yan, Xudong Huang, Guanyu Lin, Wei Li, Zhijun Tu, Hailin Hu, Jie Hu, and Yunhe Wang. Genimage: A million-scale benchmark for detecting ai-generated image. *Advances in Neural Information Processing Systems*, 36, 2024.

This appendix provides supplementary details and additional analyses. Section A describes the implementation setup; Section B reports more ablation studies; and Section C presents a comparative TDE analysis with both statistical and visual demonstrations.

A Implementation Details

Implementation of RPR. In Randomized Patch Reconstruction (RPR), diffusion-reconstructed real images are replaced with their original counterparts on a patch-wise basis. For consistency, we use Stable Diffusion v1 (SDv1) as the reconstruction model and reconstruct real images in the training subset of SDv1.4 from both GenImage and DRCT. The reconstruction is performed with the inpainting pipeline (50 denoising steps, guidance scale 7.5) using an empty prompt, a zero-filled mask of the same size as the input image, and the original image as inputs.

Implementation of PCL. Patch-wise Contrastive Learning (PCL) introduces moderate computational overhead. Training a LoRA model with only binary cross-entropy (BCE) loss on CLIP-Large requires 16 GB of GPU memory, while incorporating the margin-based contrastive loss increases memory usage to 19 GB. Similarly, training one epoch on GenImage with an NVIDIA V100 GPU increases the runtime from 3 to 4 hours.

B Additional Ablation Studies

We investigate the impact of different contrastive losses applied to embedded patch tokens. Two widely used losses are considered: InfoNCE and the margin-based contrastive loss. InfoNCE maximizes similarity between positive pairs while minimizing it for negative pairs, typically formulated as:

$$\mathcal{L}_{\text{q}} = -\log \frac{\exp(q \cdot k_+/\tau)}{\sum_{i=0}^{N} \exp(q \cdot k_i/\tau)}$$

where q and k_+ denote the embeddings of the sample and its positive counterpart, and τ is a temperature parameter. InfoNCE requires computing similarities between each sample and all negative samples, resulting in a computational complexity that grows quadratically with batch size.

In contrast, the margin-based contrastive loss, constrains the Euclidean distance between sample pairs by pulling positive pairs closer and pushing negative pairs apart with a margin α:

$$\mathcal{L}_{contrastive} = \sum_{i,j:\ i \neq j} \left[Y \cdot d_{ij}^2 + (1 - Y) \cdot \max(0, \alpha - d_{ij}^2) \right]$$

where $d_{ij} = \|\text{Emb}_{\text{pat}}^i - \text{Emb}_{\text{pat}}^j\|_2$ is the Euclidean distance between embedded patch tokens, and Y is an indicator function that equals 1 if the pair shares the same label and 0 otherwise. This loss only penalizes negative pairs whose distance is less than the margin, thus avoiding computations over all negative pairs and reducing the overall computational cost. The d_{ij} could also use the cosine distance, which is also compared in our experiments.

Impact of loss function. Tab. 6 illustrates the effectiveness of these loss functions. Unless otherwise specified, all experiments reported in the appendix are conducted on the GenImage dataset, and performance is measured using mean accuracy (mAcc).

Impact of randomized patch reconstruction vs. fixed position reconstruction Our randomized patch reconstruction method employs a random selection process for image reconstruction, allowing fake patches to appear in different regions across the entire image. Alternatively, replacing patches at fixed positions also yields images composed of both real and synthetic elements. Tab. 7 illustrates the effectiveness of randomized patch reconstruction compared to fixed-position reconstruction, both of which leverage patch-wise contrastive learning.

Table 6: The impact of contrastive loss choice.

Loss	Midjourney	SDv1.4	SDv1.5	ADM	GLIDE	Wukong	VQDM	BigGAN	mAcc
Infonce/tau=0.5	93.1	99.4	99.5	89.8	96.0	99.5	99.4	89.6	95.8
Margin/cosine	92.8	99.7	99.5	82.3	91.5	99.7	91.5	85.6	92.8
Margin/euclidean	94.8	98.5	98.3	94.7	96.1	98.6	98.5	98.0	**97.2**

Table 7: The impact of random patch replacement vs. fixed position replacement.

Position	Midjourney	SDv1.4	SDv1.5	ADM	GLIDE	Wukong	VQDM	BigGAN	mAcc
Upper Half	87.1	99.7	99.6	83.9	94.5	99.7	99.2	96.0	95.0
Lower Half	87.5	99.7	99.6	81.7	93.4	99.7	99.1	94.6	94.4
Left Half	87.7	99.8	99.5	84.4	93.8	99.7	99.0	90.6	94.3
Right Half	81.6	99.8	99.7	74.8	79.6	99.8	98.7	86.2	90.0
Random	94.8	98.5	98.3	94.7	96.1	98.6	98.5	98.0	**97.2**

Table 8: The impact of patch size of random patch replacement.

Patch Size	Midjourney	SDv1.4	SDv1.5	ADM	GLIDE	Wukong	VQDM	BigGAN	mAcc
112	99.6	99.3	92.3	92.7	99.5	95.8	99.5	94.3	96.6
56	99.4	99.2	93.8	90.8	99.4	95.8	99.1	97.2	96.8
28	98.7	98.3	95.7	95.4	98.8	97.5	98.5	98.1	**97.6**
14	94.8	98.5	98.3	94.7	96.1	98.6	98.5	98.0	<u>97.2</u>

Table 9: The impact of random patch replacement vs. random patch dropout.

Dropout Rate	Midjourney	SDv1.4	SDv1.5	ADM	GLIDE	Wukong	VQDM	BigGAN	mAcc
0.10	71.3	99.9	99.8	67.9	82.7	99.8	97.3	77.0	88.5
0.15	94.3	98.7	98.6	87.9	90.4	98.7	98.5	90.9	<u>94.2</u>
0.20	77.0	99.9	99.8	69.2	72.0	99.8	98.7	87.7	89.1
0.25	77.2	99.9	99.8	71.1	74.7	99.8	98.6	89.3	90.2
Replacement	94.8	98.5	98.3	94.7	96.1	98.6	98.5	98.0	**97.2**

Impact of patch size of randomized patch reconstruction Our randomized patch reconstruction method reconstructs real images into fake counterparts where the patch size may influence performance. with patch size potentially influencing performance. Using patches of size 14×14 is intuitive, as it aligns with the token size used in Vision Transformers (ViTs). Tab. 8 illustrates that the training process is not sensitive to reconstruction patch size, and smaller patch sizes are preferred.

Impact of randomized patch reconstruction vs. random patch dropout Our randomized patch reconstruction method involves substituting fake image patches with their real counterparts, thereby compelling the model to exploit more artifacts from the remaining patches. An alternative approach shown in Fig. 9 is random patch dropout, in which certain patches are removed, resulting in images with fewer patches. Tab. 9 illustrates the effectiveness of Randomized Patch Reconstruction, by comparing patch reconstruction with patch dropout at various dropout rates, with both methods employing patch-wise contrastive learning. The results indicate that, with an appropriate dropout ratio, patch dropout also achieves favorable performance, supporting our hypothesis that models tend to over-rely on a subset of patches. Dropout thus serves as a remedy for this issue. However, patch dropout underperforms patch reconstruction, possibly because patch reconstruction preserves the overall appearance and input domain of the image (i.e., a complete image rather than a masked one), thereby increasing the task's difficulty.

C More TDE Comparative Analysis

TDE distribution of different subsets of GenImage To better analyze the models' ability to leverage all patches from an image, we use TDE to count the contribution of patch$_{(i,j)}$, which can be

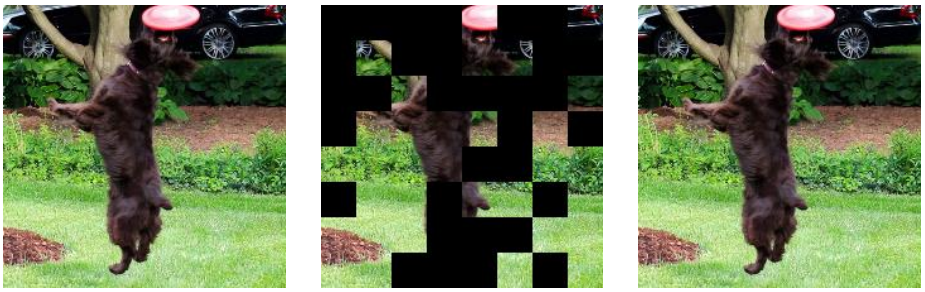

a) Input Image | b) Image with Random Mask | c) Input Image with RPR

Figure 9: Visual comparison between random patch dropout (masking) and reconstruction. It is evident that, by reconstruction, the overall visual appearance remains unchanged.

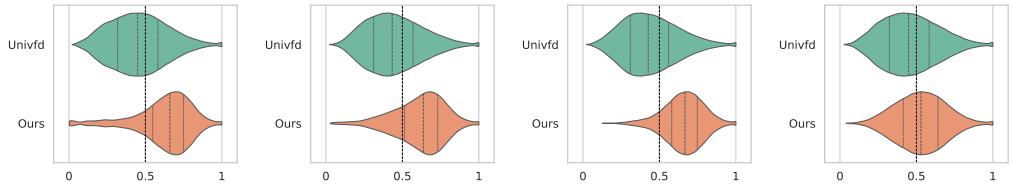

(a) SDv1.4 (b) VQDM (c) BigGAN (d) Glide

Figure 10: TDE distribution on different generators of ours and UnivFD.

defined as the difference in logits at the (i, j) position of an image before and after being masked. Fig. 10 illustrates the TDE distribution of UnivFD and our method. For better statistical analysis, we normalize the TDE values to a range $[0, 1]$ using the exponential function $e^{TDE_{(i,j)}-TDE_{max}}$. This normalization facilitates the measurement of differences between less dominant patches and the most dominant patches in the images. The figure demonstrates that a greater number of patches from our method are more uniform.

Visual Showcase of TDE distribution of different subsets on GenImage To better showcase our model's better ability to leverage all patches from an image, we present a visual analysis of TDE across various subsets of the GenImage dataset. The GenImage dataset is divided into multiple subsets, each representing distinct image generation methods. These subsets include GAN-based models such as BigGAN, and diffusion-based models, including Stable Diffusion, VQDM, and ADM. Due to space limitations in the main text, we showcased limited images; here, we present most subset models of GenImage: the diffusion-based Stable Diffusion v1.4 (Fig. 11), the closed-source Midjourney (Fig. 12), and the GAN-based BigGAN (Fig. 13). The rest diffusion-based model are from Fig. 14 to Fig. 16.We use CLIP as backbone for our visualization.

D THE USE OF LARGE LANGUAGE MODELS (LLMS)

In this paper, we only use the large language model to help polish our text. The large language model has no role in the research conception.

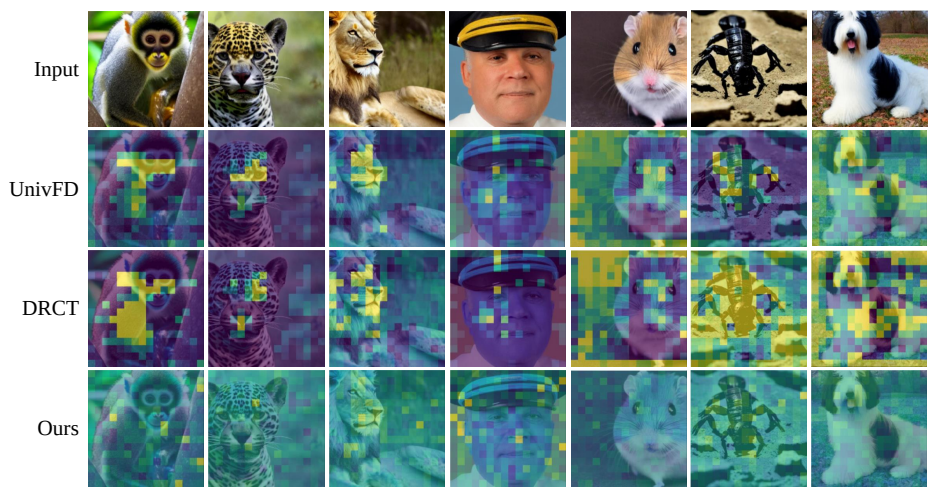

Figure 11: Showcase of TDE map on SDv1.4. Images are sourced from GenImage (Zhu et al., 2024).

Figure 12: Showcase of TDE map on Midjourney. Images are sourced from GenImage (Zhu et al., 2024).

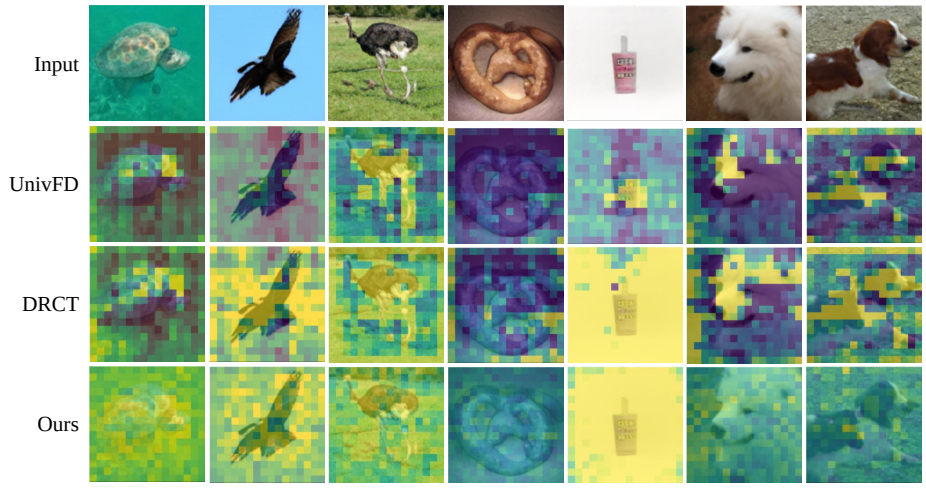

Figure 13: Showcase of TDE map on BigGAN. Images are sourced from GenImage (Zhu et al., 2024).

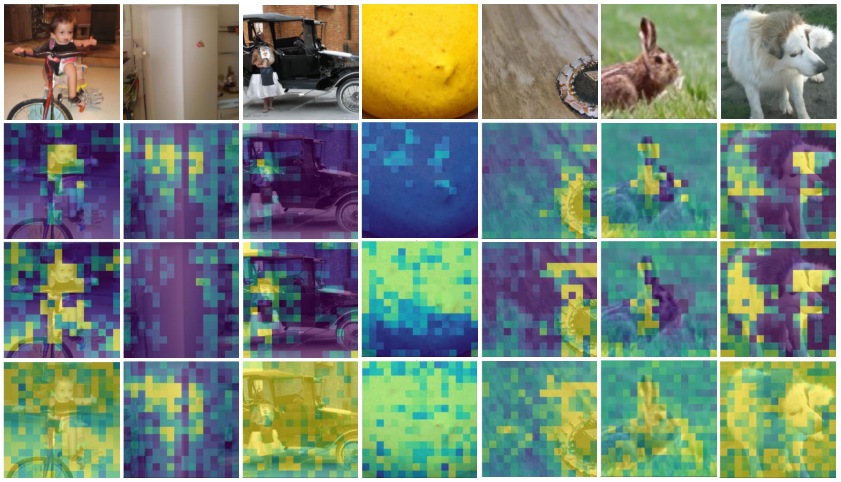

Figure 14: Showcase of TDE map on ADM. Images are sourced from GenImage (Zhu et al., 2024).

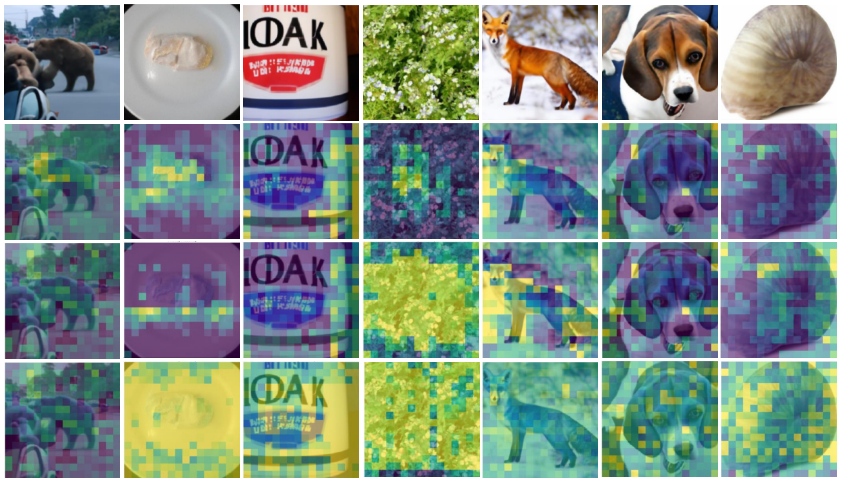

Figure 15: Showcase of TDE map on Glide. Images are sourced from GenImage (Zhu et al., 2024).

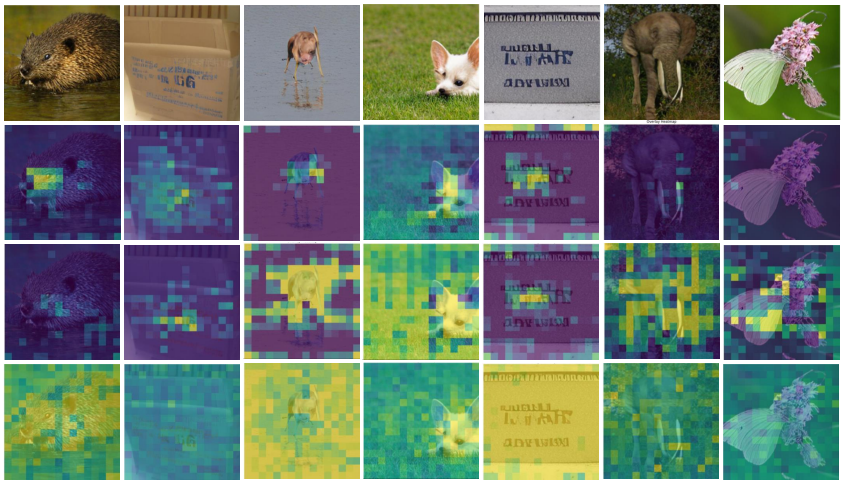

Figure 16: Showcase of TDE map on VQDM. Images are sourced from GenImage (Zhu et al., 2024).